ADVANCED ENERGY MATERIALS

www.advenergymat.de

Highly Efficient Ambient Temperature CO_2 Photomethanation Catalyzed by Nanostructured RuO_2 on Silicon Photonic Crystal Support

*Abdinoor A. Jelle, Kulbir K. Ghuman, Paul G. O'Brien, Mohamad Hmadeh, Amit Sandhel, Doug D. Perovic, Chandra Veer Singh, Charles A. Mims, and Geoffrey A. Ozin**

Sunlight-driven catalytic hydrogenation of CO_2 is an important reaction that generates useful chemicals and fuels and if operated at industrial scales can decrease greenhouse gas CO_2 emissions into the atmosphere. In this work, the photomethanation of CO_2 over highly dispersed nanostructured RuO_2 catalysts on 3D silicon photonic crystal supports, achieving impressive conversion rates as high as 4.4 mmol g_{cat}^{-1} h^{-1} at ambient temperatures under high-intensity solar simulated irradiation, is reported. This performance is an order of magnitude greater than photomethanation rates achieved over control samples made of nanostructured RuO_2 on silicon wafers. The high absorption and unique light-harvesting properties of the silicon photonic crystal across the entire solar spectral wavelength range coupled with its large surface area are proposed to be responsible for the high methanation rates of the RuO_2 photocatalyst. A density functional theory study on the reaction of CO_2 with H_2 revealed that H_2 splits on the surface of the RuO_2 to form hydroxyl groups that participate in the overall photomethanation process.

1. Introduction

Carbon dioxide utilization as a chemical feedstock to produce value-added chemicals and fuels is a promising endeavor that has the potential to provide sustainable energy security and address several global challenges including climate change and environmental protection.[1–13] Among the different ways of utilizing CO_2, gas-phase CO_2 reduction has gained huge interest due to its technological and economic feasibility for large-scale fuel production.[14–16] In the literature, several catalysts have been studied for the reduction of CO_2 to produce various chemical feedstocks and fuels.[17–20] One of the most desirable fuels obtained from the reduction of CO_2 through the Sabatier reaction ($CO_2 + 4H_2 \rightarrow CH_4 + 2H_2O$) is methane, which is widely used for both domestic and industrial applications.[21,22] The most commonly used catalysts to drive the Sabatier reaction are based on ruthenium[23–26] and nickel;[27–30] although several other catalysts have also been investigated.[31–34] Traditionally, the Sabatier reaction had been thermally driven until Thampi et al. reported that it can also be activated photochemically with solar simulated irradiation using Ru/RuO_x loaded on TiO_2.[35] A more thorough investigation of this reaction demonstrated that it was catalyzed photothermally.[36] Thereafter, several different photocatalysts have been developed for the photomethanation of CO_2. An interesting example is the complete photocatalytic reduction of CO_2 to CH_4 by H_2 under solar-simulated irradiation achieved with a Ni/silica-alumina photocatalyst.[37] Recently, we reported on gas-phase photomethanation of CO_2 over Ru sputtered on vertically aligned silicon nanowires (black silicon) and were able to obtain CH_4 production rates as high as 1 mmol g_{cat}^{-1} h^{-1} under solar simulated light using visible and near-infrared photons.[38] The high photomethanation rate was ascribed to the enhanced light absorption provided by the black silicon support. Subsequently, we also developed a hybrid photocatalyst consisting of defect-engineered indium oxide nanostructures coated on the black silicon support that efficiently converts CO_2 into CO under simulated solar irradiation and found that superior light-harvesting properties coupled with minimal light reflectance losses exhibited by the black silicon support were instrumental

Dr. A. A. Jelle, Prof. K. K. Ghuman, Prof. D. D. Perovic, Prof. C. V. Singh
Department of Materials Science and Engineering
University of Toronto
184 College Street, Toronto, Ontario M5S 3E4, Canada
Prof. P. G. O'Brien
Department of Mechanical Engineering
Lassonde School of Engineering
York University
Toronto, Ontario M3J 1P3, Canada
Prof. M. Hmadeh
Department of Chemistry
Faculty of Arts and Sciences
American University of Beirut
P.O. Box 11-0236, Beirut, Lebanon
A. Sandhel, Prof. G. A. Ozin
Materials Chemistry and Nanochemistry Research Group
Solar Fuels Cluster
Department of Chemistry
University of Toronto
80 St. George Street, Toronto, Ontario M5S 3H6, Canada
E-mail: gozin@chem.utoronto.ca
Prof. C. A. Mims
Department of Chemical Engineering and Applied Chemistry
University of Toronto
200 College St., Toronto, Ontario M5S 3E5, Canada
The ORCID identification number(s) for the author(s) of this article can be found under https://doi.org/10.1002/aenm.201702277.

DOI: 10.1002/aenm.201702277

in enhancing the CO_2 reduction rates.[39] Additionally, we showed that the hybrid photocatalyst was able to utilize both light (photochemically) and heat (photothermally) to drive the photoreduction of CO_2 to CO. These studies highlight the importance of the support material, which is critical for providing better catalyst dispersion and stability to sintering, and enhanced light absorption properties. It is therefore important for achieving efficient sunlight-driven CO_2 reduction reactions to rationally select and design a support material that is able to absorb most of the solar spectrum from the UV to the near-infrared region. Silicon is the natural choice, with an electronic band gap of 1.1 eV, enabling absorption of over 80% of the solar spectrum.

In this study, we expand and enrich upon this strategy by exploring for the first time the gas-phase photomethanation of CO_2 using a silicon inverse opal as a photonic crystal support for nanostructured RuO_2 driven by high-intensity simulated solar irradiation from a 300 W Xe lamp. Inverse opal photonic crystals have recently gained huge interest in photocatalytic applications due to their superior light-harvesting properties by controlling the way light propagates through these materials. For example, Chen et al. showed enhanced photoactivity of inverse opal TiO_2 in the photooxidation of methylene blue.[40] This enhanced photoactivity was due to slow photons with energies close to the electronic band gap of TiO_2, which increased the path length of light allowing it to be absorbed more efficiently. Moreover, Ramiro-Manzano et al. have shown that dye-sensitized photoelectrochemical solar cells comprising of a photonic sponge architecture could be used to efficiently trap light and harvest photons in the near-UV and visible region of the solar spectrum.[41] In addition, Li et al. have demonstrated enhanced photocatalytic activity of inverse opal photonic crystal TiO_2 whereby the stop band and multiple scattering effects both contributed to greatly improve the light-harvesting properties of the material leading to its superior photocatalytic activities.[42] Several other studies have also reported enhanced photocatalysis by inverse opal materials enabled by the slow photon effect.[43–48]

Inspired by the photocatalytic attributes of inverse opal photonic crystal supports, we employed a novel solution phase synthetic route to nucleate and grow RuO_2 nanocrystals on a silicon inverse opal photonic crystal, which we denote as $ncRuO_2$/i-Si-o, and examined its catalytic activity toward the photomethanation of CO_2. Notably we achieved an impressive photomethanation rate as high as 4.4 mmol g_{cat}^{-1} h^{-1} under solar simulated light focused to an intensity of ≈22 kW m^{-2} (≈22 sun) with no external heating. This rate represents a significant improvement over the RuO_2 nanocrystals deposited on planar silicon wafers ($ncRuO_2$/SiW) and tested under the same reaction conditions. Furthermore, isotope tracing experiments using $^{13}CO_2$ were performed to confirm that the CH_4 products did not originate from adventitious carbon sources. The bare silicon inverse opal photonic crystal support is not active toward the methanation of CO_2 in the light or dark. Moreover, we performed density functional theory (DFT) calculations to understand the interaction of the reactant CO_2 and H_2 molecules with the surface of the catalyst and gain atomistic insight into the overall methanation reaction mechanism.

2. Results and Discussion

In this study, we used a 3D photonic crystal in the form of an inverted silicon opal (i-Si-o) as a substrate for RuO_2 nanocrystals and investigated the gas-phase photomethanation of CO_2 under solar simulated light. The i-Si-o sample was fabricated by infiltrating the interstitial voids of silica spheres with silicon using dynamic chemical vapor deposition. The silica spheres were later removed by etching them in a solution containing HF/H_2O. This procedure was described in our previous work.[49] The RuO_2 nanocrystals were then deposited on the i-Si-o support using a wet chemical deposition technique to form $ncRuO_2$/i-Si-o (see the Experimental Section for details). Scanning electron microscopy (SEM) images of the resulting $ncRuO_2$/i-Si-o catalysts are shown in **Figure 1**, which show that the RuO_2 nanocrystals are well dispersed on the i-Si-o structure thus providing a large surface area and stability toward sintering. Furthermore, the porous structure of the i-Si-o facilitates a high degree of contact between the nanocrystalline catalysts and the reactant gases CO_2 and H_2. The average diameter and mass of the RuO_2 nanocrystals dispersed on the i-Si-o supports were determined to be 24 nm and 318 μg cm^{-2}, respectively (Figure S1a, Supporting Information). As a reference sample, we deposited RuO_2 nanocrystals on a silicon wafer, $ncRuO_2$/SiW (Figure S1b, Supporting Information). The average size of the RuO_2 nanocrystals on the silicon wafer is ≈45 nm, almost twice the size but nearly the same mass as the RuO_2 loaded on the inverse photonic crystal. We were able to adjust the reaction conditions and tune the particle sizes for optimizing the conversion rates. As a result, another $ncRuO_2$/SiW sample with an average particle size of ≈20 nm similar to the one deposited on the photonic crystal was prepared as shown in Figure S1c,d (Supporting Information) but only a small amount of RuO_2 nanoparticles (NPs) could be deposited. Hence, we used the ≈45 nm RuO_2/SiW sample shown in Figure S1b (Supporting Information) as a reference. In addition, we used X-ray photoelectron spectroscopy (XPS) measurements to determine the chemical state of the ruthenium deposited onto the i-Si-o support. These data are presented in Figure S2 (Supporting Information) and show the survey spectrum and the core-levels for Ru 3d, Ru 3p, and Si 2p of the $ncRuO_2$/i-Si-o sample before and after the photomethanation reaction. The binding energies of the Ru $3d_{5/2}$ and Ru $3d_{3/2}$ spin–orbit components are at 280.7 and at 284.9 eV, respectively, confirming the existence of Ru(IV) in RuO_2 nanocrystals.[50] Moreover, XPS measurements performed before and after the testing revealed that the chemical state of ruthenium of the RuO_2 nanocrystals did not change during the Sabatier reaction (Figure S2, Supporting Information). Because of the interference from the C 1s peak that appears close to Ru 3d, it is generally a good idea to use other photoemission peaks to further confirm the chemical nature of the deposited RuO_2 nanocrystals. To this end, we have measured Ru 3p core-levels of the $ncRuO_2$/i-Si-o sample (Figure S2c, Supporting Information). This gives the binding energy of the $3p_{3/2}$ peak as 463.8 eV, which is assigned to the Ru(IV) of RuO_2.[51] Figure S2d (Supporting Information) displays the Si 2p spectrum of the $ncRuO_2$/i-Si-o sample, which shows that the surface of i-Si-o is oxidized as SiO_2. Similarly, XPS measurements of the $ncRuO_2$/SiW sample showed the formation of the

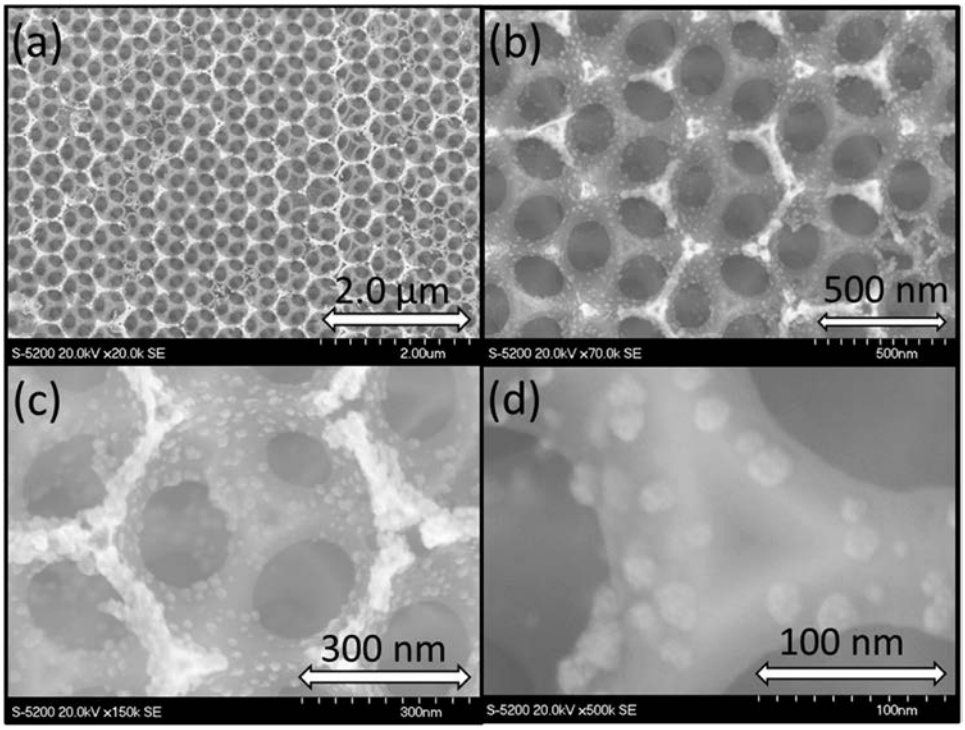

Figure 1. SEM secondary electron images of $ncRuO_2$/i-Si-o sample under different magnifications: a) 20×, b) 70×, c) 150×, and d) 500×.

RuO_2 nanocrystals on the silicon wafer. Figure S3 (Supporting Information) depicts Ru 3d and 3p core-levels of $ncRuO_2$/SiW sample, which are consistent with the formation of RuO_2.

After characterization of the samples with XPS, their photocatalytic activities were measured by evaluating the gas-phase photomethanation reaction between CO_2 and H_2. The samples used in the photocatalytic testing were cut into 1 × 1 cm squares. The photocatalytic measurements were performed using a custom-built batch reactor made of stainless steel with a quartz window. The reactor was filled with a stoichiometric mixture of $^{13}CO_2$ and H_2 (1:4) to a pressure of 2 atm. The Sabatier reaction rate of the $ncRuO_2$/i-Si-o sample was measured and compared to that of the reference sample $ncRuO_2$/SiW under solar simulated light from a 300 W Xe lamp, focused to an intensity of ≈22 kW m^{-2} (≈22 sun) without any external heating. For comparison, the Sabatier reaction rates of these two samples in the dark with external resistive heating were also measured and are plotted in **Figure 2**. The purple bars represent tests performed using high-intensity Xe lamp illumination whereas the black bars represent the tests performed in the dark. Clearly, the methanation rate over the $ncRuO_2$/i-Si-o under illumination is significantly higher than that performed in the dark. The photomethanation rate of the $ncRuO_2$/i-Si-o sample under illumination is 4.4 mmol g_{cat}^{-1} h^{-1} compared to 0.5 mmol g_{cat}^{-1} h^{-1} in the dark at 170 °C, which is nine times higher. However, the Sabatier reaction proceeds at a similar rate over the $ncRuO_2$/SiW sample both in the dark (0.2 mmol g_{cat}^{-1} h^{-1}) and under full illumination (0.4 mmol g_{cat}^{-1} h^{-1}). Moreover, comparing the methanation rates of both samples under illumination, we find that the methanation rate of the $ncRuO_2$/i-Si-o sample (4.4 mmol g_{cat}^{-1} h^{-1}) is significantly higher than that of the $ncRuO_2$/SiW sample (0.4 mmol g_{cat}^{-1} h^{-1}) by a factor of 11. Because RuO_2 is the active catalyst, the photomethanation rates are normalized to the weight of the RuO_2 nanocrystals. More importantly, the Sabatier reaction rates did not decrease after the $ncRuO_2$/i-Si-o sample had been tested for 30 h (Figure S4, Supporting Information) indicating that the catalyst did not deactivate with time. It should be mentioned that a very small amount of CO product was observed in the gas chromatograph (GC) during the photocatalytic testing of the samples. The CO is mainly a reaction intermediate because CO_2 methanation usually goes through the reverse water gas shift (RWGS) reaction $CO_2 + H_2 \leftrightarrow CO + H_2O$, followed by further CO hydrogenation. The gas chromatography mass spectroscopy (GC-MS) spectra of the detected CO are shown in Figure S12 (supporting information).

Key factors that could contribute to the enhanced photomethanation rates over the $ncRuO_2$/i-Si-o sample were investigated. First, we considered whether the enhanced methanation rate of the $ncRuO_2$/i-Si-o sample is due to the relatively smaller size of the RuO_2 nanocrystals on the silicon photonic crystal compared to the ones deposited on the silicon wafer (Figure S1, Supporting Information). To this end, the RuO_2 deposition technique of the $ncRuO_2$/SiW sample was tailored so that different sizes of RuO_2 nanocrystals (in the range of 10–50 nm) could be deposited on the silicon wafer. It should be noted that due to the limited surface area of the silicon wafer support compared to the i-Si-o support, it is not possible to simultaneously deposit the same particle size and particle loading of $ncRuO_2$ on the silicon wafer as that on the i-Si-o support. However, we measured methanation rates of $ncRuO_2$/SiW sample as a function of $ncRuO_2$ particle size and particle loading and the rates remained very similar to that presented in Figure 2

indicating that the sizes and loadings of RuO_2 nanocrystals of the $ncRuO_2$/SiW samples did not have significant impact on the rate of photomethanation. Second, there is a large difference in surface area between the two samples. While the silicon wafer is flat, the inverse opal photonic crystal with large voids provides a large surface area for RuO_2 nanocrystal deposition and could be the key to the observed enhanced photomethanation rates in contrast to the low surface area of the silicon wafer. Furthermore, the fact that the rate of methanation under high-intensity illumination is an order of magnitude higher in the $ncRuO_2$/i-Si-o sample compared to the $ncRuO_2$/SiW sample is due to the inherent optical property of the silicon inverse opal photonic crystal. It is well known in the literature that 3D silicon photonic crystals can be used to increase light absorption over certain spectral regions by scattering and increasing the path length of light that propagates through the material.[52] The superior optical absorption properties of the i-Si-o resulting from light scattering are expected to play an important role in absorbing the majority of the incident photons in the UV–visible and near-infrared region of the solar spectrum compared to the silicon wafer, which reflects most of the incident photons in these regions of the solar spectrum. To this end, the diffuse reflectance and absorption of both samples were measured and the result is shown in Figure S5 (Supporting Information). It can be seen from Figure S5a (Supporting Information) that the $ncRuO_2$/i-Si-o sample reflects less of the incident photons in the UV–visible and near-infrared region of the solar spectrum compared to the $ncRuO_2$/SiW sample. This low reflectance of the $ncRuO_2$/i-Si-o sample translates to higher absorption (an average of 80%) particularly in the UV–visible region where the incoming photons are most energetic as can be seen in Figure S5b (Supporting Information). These absorbed incident photons produce photogenerated electrons and holes, which mainly recombine and thermalize producing heat energy that drives the Sabatier reaction photothermally. It is possible that some of these photogenerated charges may interact with the reactant species and drive the Sabatier reaction photochemically but we believe the majority of them thermalize and produce heat that drives the reaction photothermally. The evidence of this comes from the temperature profile of the samples, which was monitored during the photomethanation testing. As depicted in Figure S6 (Supporting Information), the temperature of both samples rapidly increased once the Xe lamp was turned on and remained fairly constant throughout the test until the Xe lamp was turned off. The $ncRuO_2$/i-Si-o sample reached ≈170 °C while the $ncRuO_2$/SiW sample reached only up to 150 °C under the same illumination conditions. While both samples were exposed to the same number of incident photons, the $ncRuO_2$/i-Si-o sample absorbs more photons producing electrons and holes that recombine nonradiatively and produce thermal energy required to drive the Sabatier reaction photothermally. In addition to the superior optical properties of the silicon photonic crystal that results in the enhanced photomethanation rates, the $ncRuO_2$ can also contribute to the observed higher photomethanation rates. RuO_2 is a metal oxide with metallic electronic properties arising from the partially filled Ru 4d states and has the rutile crystal structure. It has broad and intense diagnostic conduction electron plasmon resonance, which spans the wavelength range 600–2000 nm.[53] This allows the absorption of visible and near-infrared light originating from interband p-d and intraband d-d transitions.[53–55] Therefore, it is likely that the catalyst RuO_2 plasmons and support i-Si-o phonons both provide their individual photothermal effects, which can enhance the rate of the Sabatier reaction, to different extents. Further studies will be required to deconvolute the effect each of these have on the observed rates.

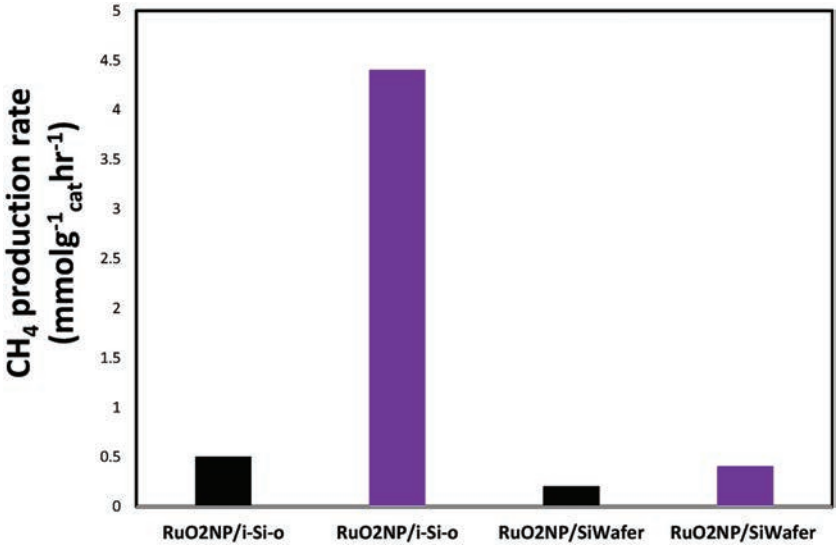

Figure 2. $^{13}CH_4$ production rate of $ncRuO_2$/i-Si-o and $ncRuO_2$/SiW hybrid samples. The samples that are tested under high-intensity Xe lamp illumination (22 kW m^{-2}) without external heating are shown in purple color while the black bars correspond to experiments done in the dark at 150 and 170 °C for sample $ncRuO_2$/SiW and $ncRuO_2$/i-Si-o, respectively.

In order to further understand the enhanced photomethanation rate of CO_2 by the $ncRuO_2$/i-Si-o sample, we performed a wavelength-dependent study where we used high-pass cut-off filters and analyzed the different temperatures reached by each test and compared the resulting photomethanation rates. The Sabatier reaction rate over the $ncRuO_2$/i-Si-o catalyst was measured under illumination from a 300 W Xe lamp with a 625 nm high-pass filter, a 495 nm high-pass filter, and without a filter and the results are plotted as tests 1, 2, and 3 in **Figure 3**a, respectively. The measured Sabatier reaction rates for Tests 1, 2, and 3 are 0.2, 0.8, and 4.4 mmol g_{cat}^{-1} h^{-1}, respectively, normalized to the weight of the RuO_2. The relative intensity of the incident light spectra for Tests 1, 2, and 3 are 1.8, 5.0, and 22 kW m^{-2}, respectively. The spectral irradiance that is incident on the three tests is shown in Figure S7 (Supporting Information). This trend in photomethanation rates for the three tests is closely correlated with the $^{13}CH_4$ mass spectrum ion peak in Figure 3b. Test 1 had the lowest $^{13}CH_4$ peak and Test 3 had the highest $^{13}CH_4$ mass peak. We have also monitored the temperature profiles of these three tests (Figure 3c). The highest temperature was reached during Test 3 with an average

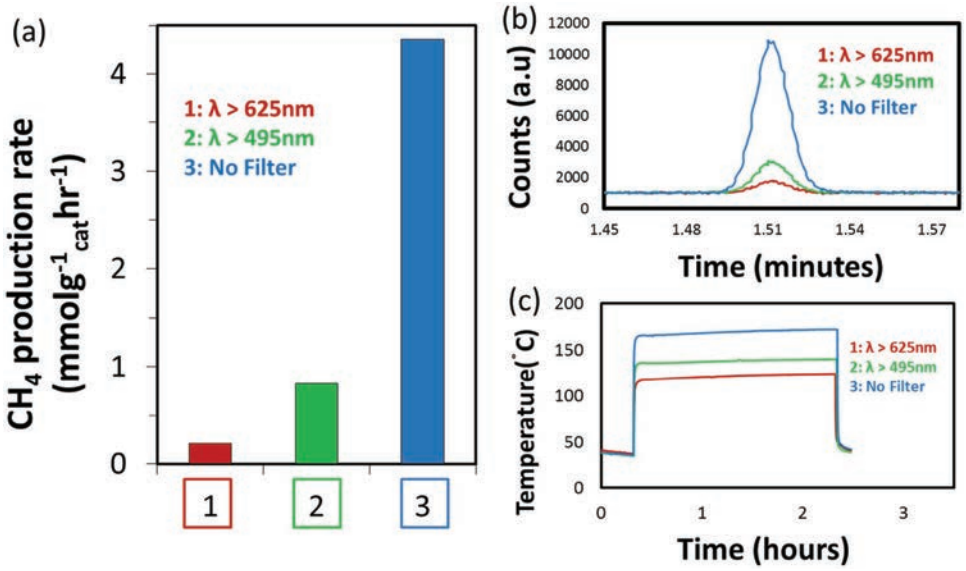

Figure 3. a) Photomethanation rate over the ncRuO$_2$/i-Si-o catalyst tested under different illumination conditions; for Test 1 the incident light spectra from the Xe lamp were passed through a 625 nm high-pass cut-off filter, for Test 2 a 495 nm high-pass cut-off filter was used, and no filter was used for Test 3. The relative intensity of the incident light spectra for Tests 1, 2, and 3 are 1.8, 5.0, and 22 kW m^{-2}, respectively. b) GC–MS spectra ion mass 17 peak for the three photomethanation tests carried out over the ncRuO$_2$/i-Si-o sample. c) Temperature profiles recorded for the three batch reaction tests.

of 170 °C while the lowest temperature was reached during Test 1 with an average temperature of 122 °C. Test 2 reached an average temperature of 138 °C. The photomethanation rates plotted in Figure 3a together with the temperature profiles in Figure 3c clearly show the i-Si-o support heats up under high-intensity illumination. The thermal energy produced is then transferred to the attached RuO_2 nanocrystals, which drives the reaction photothermally. Additionally, it is observed that the photomethanation rate of Test 2 is higher than the photomethanation rate of the same sample tested under resistive heating of 170 °C in the dark (0.8 mmol g_{cat}^{-1} h^{-1} vs 0.5 mmol g_{cat}^{-1} h^{-1}). Yet, Tests 2 registered a lower average temperature of 138 °C during the photomethanation tests. This indicates that the incident photons impinging on the photonic crystal do not just provide thermal energy required to activate the Sabatier reaction but could also cause local heating of the nanocrystalline RuO_2 catalyst on the i-Si-o support, derived from the photothermal effect, which provides an additional driving force beyond that of the thermodynamically defined exothermicity of the reaction. Moreover, the photomethanation reaction could further be activated photochemically. The photons that enhance Sabatier reaction photochemically may only be a small fraction of the total incident photons irradiated on the sample.[36] From this wavelength-dependent study, we conclude that photomethanation rates increase with increasing relative intensity of incident photons.

For efficient photomethanation, it is necessary to remove the biproduct H_2O produced during the photomethanation process from the active sites. At relatively low temperatures, the water biproduct has a negative impact on the exothermic Sabatier reaction mainly because it tends to adsorb on the active sites inhibiting further methanation reaction taking place at the active sites. The temperature required to completely remove the H_2O biproduct is ≈147 °C,[56] which to some extent explains the very low methanation rates of Test 1 and Test 2 compared to Test 3. On the other hand, the presence of water has been found to be advantageous as it suppresses carbon deposition because it impedes side reactions such as ($C + 2H_2O \leftrightarrow CO_2 + 2H_2$) that are selectively activated especially at elevated temperatures.[57–59] This carbon deposition side reaction leads to catalyst poisoning.

In the literature, the mechanistic details of CO_2 methanation over ruthenium-based materials are highly debated. It is not clear whether CO_2 is adsorbed on the catalyst first followed by the hydrogenation of the adsorbed species to produce CH_4[60,61] or CO_2 directly dissociates on the surface of the catalyst into adsorbed CO_{ad} and O_{ad} which is then hydrogenated to form CH_4.[62,63] Several factors such as temperature, reactant gas ratios, and type of supports used are responsible for the different mechanisms.[64,65] In either case, the hydrogenation step is the rate-limiting step. The most reported ruthenium-based Sabatier reaction catalysts consist of metallic ruthenium supported on metal oxides such as TiO_2.[23,61,66–68] During the Sabatier reaction, hydrogen splits on the ruthenium metal and methanation take place at the interface between the metal and the support.[61] Whereas metallic ruthenium can readily form surface metal hydrides, which facilitates methanation, very little is known about the methanation details of RuO_2. Carenco et al. investigated the active state of 2 nm supported RuO_2 on TiO_2 (RuO_2/TiO_2). Using ambient-pressure X-ray photoemission spectroscopy, they concluded that the active state is indeed metallic ruthenium, which resulted from the reduction of the RuO_2 in a hydrogen environment.[69] While RuO_2 can be reduced in a hydrogen environment, we do not expect our RuO_2 to be greatly reduced due to the large size of the nanocrystals used and the low temperature reaction conditions

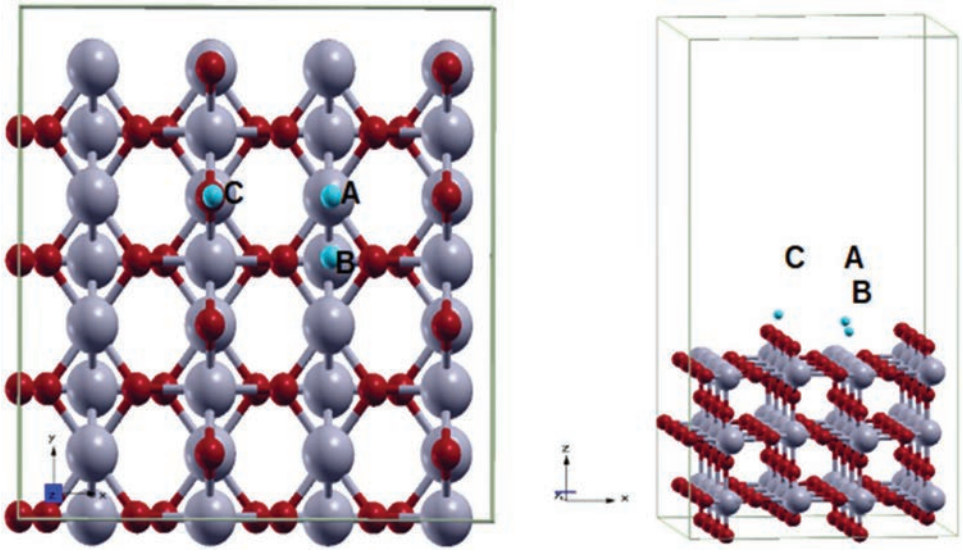

Figure 4. Top view (left) and side view (right) of RuO_2(110) surface. A, B, and C represent the various absorption sites considered for the calculation. A: top of fivefold coordinated Ru, B: bridge site, and C: on top of twofold coordinated O. Color code: Ru, gray and O, red.

employed. Furthermore, XPS measurement performed after the tests confirmed that the oxidation state of the Ru remained at +4 indicating that the RuO_2 was not reduced to metallic Ru (Figure S2, Supporting Information).

Accordingly, we propose that the photomethanation reaction on the ncRuO_2/i-Si-o catalyst begins with the splitting of H_2 on the surface of the RuO_2 to form hydroxyl groups as a result of the interaction of H_2 with the oxygen of the RuO_2. Then CO_2 interacts with hydroxyl groups to form intermediates such as formates, carbonates, and bicarbonates, which lead to the final methane product. In addition, a H_2 molecule may also interact with the oxygen of the RuO_2 to form water, which will then desorb at high temperatures to create oxygen vacancies that act as active sites for further reaction. Using XPS, we were able to identify both oxygen vacancies[17,70,71] and adsorbed water[72–74] on the surface of the catalyst as seen from the O1s peak of our photocatalyst after the photomethanation test (Figure S8, Supporting Information).

In order to gain a deeper insight into the high CO_2 methanation rates and understand the details of the interaction of the reactant gases with the surface of the highly dispersed nanocrystalline RuO_2 nanocrystals supported on the silicon inverse photonic crystal, DFT analysis was conducted. We have chosen the RuO_2(110) surface in our DFT simulations because the high-resolution transmission electron microscopy (HRTEM) image of the ncRuO_2 revealed that the RuO_2(110) is the dominant exposed surface (Figure S11, Supporting Information). Additionally, the RuO_2(110) surface is the most common and thermodynamically most stable surface among the RuO_2 surfaces.[75–78] In the DFT analysis, a seven-layer slab geometry of the most common orientation (110) of RuO_2 surface with a vacuum layer of about 20 Å was chosen, further sandwiched by the semi-infinite vacuum called the effective screening medium (ESM). The modeled system is a continuous layer, about 10 Å in thickness, which represents a nanoscale film, and captures the behavior of nonedge nanocrystal regions, which form the majority of the surface area. We treated the slab part that consists of substrate and adsorbate atoms microscopically within DFT and we treated the medium part within a continuum characterized by relative permittivity of unity. In order to incorporate the effect of photogenerated electrons and holes from the silicon substrate to the RuO_2 surface, we investigated the RuO_2(110) surface with an extra electron and an extra hole denoted by $[RuO_2(110)]^-$ and $[RuO_2(110)]^+$, respectively. The neutral RuO_2(110) surface was also simulated for comparison. Further, on the RuO_2(110) surface, there are two types of Ru atoms: the sixfold coordinated (same as bulk Ru atom) and the fivefold coordinated, and two types of O atoms: the threefold coordinated (same as bulk O atom) and the twofold coordinated. Therefore, in order to analyze the interaction of adsorbates on RuO_2(110) surface we considered site A which is on top of fivefold coordinated Ru, site B which is the bridge site, and site C which is on the top of twofold coordinated O as shown in **Figure 4**.

The interaction of one of the reactant gases, H_2 with the neutral and charged (±1,0) RuO_2(110) surfaces was first investigated. Here, H_2 was placed sufficiently far away from each of the three surfaces before optimization. The final optimized structures for the hydrogenated surfaces are shown in **Figure 5**. Bader charge[79] and bond length analysis on these optimized geometries was then performed (see Table S1, Supporting Information). This analysis showed that the H_2 molecule interacts in the same way with charged surfaces as it does with the neutral surface. On all three surfaces, H_2 is physisorbed on site A, splits and forms OH groups on site B and is chemisorbed and forms water on site C. Bader charge analysis shows that the negative surface forms more basic OH groups, having about −0.03e to −0.02e higher charge, as compared to the other surfaces. Formation of H_2O on site C leads to coordinately unsaturated Ru atoms, which can subsequently dissociate H_2 to form Ru−H bonds that participate in the Sabatier reaction. Further, H_2 interaction with adsorption site B and C leads to the formation of hydroxyl groups and adsorbed water, respectively, as seen in experimental O1s XPS spectrum in

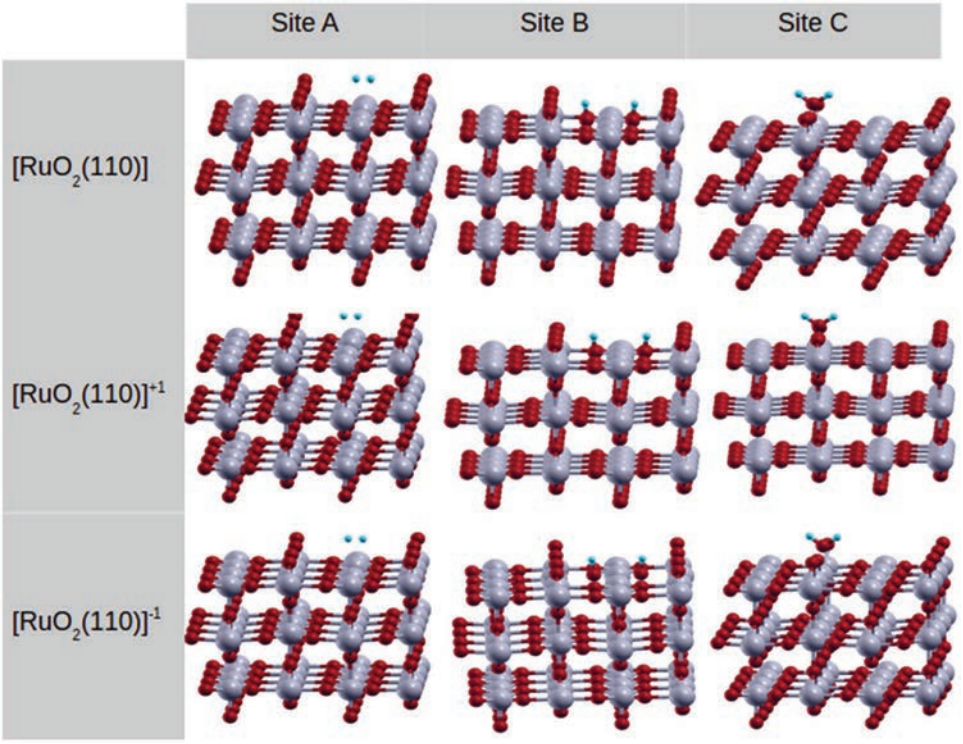

Figure 5. H_2 adsorption on various sites on neutral and charged (110) RuO_2 surfaces. A: top of fivefold coordinated Ru, B: bridge site, and C: on top of twofold coordinated O. Color code: H, blue; Ru, gray; and O, red.

Figure S8 (Supporting Information). The interaction of H_2 with the negatively charged surface results in adsorbed H_2 having an oxidation state different from when it interacts with other two surfaces (Table S1, Supporting Information). Further, the calculations done by placing CO_2 vertically as well as horizontally on all the adsorption sites showed that none of the surfaces were able to dissociate CO_2. The CO_2 molecule is adsorbed on site A and C of all the surfaces, and site B of the positively charged surface (Figure S9, Supporting Information) but it never dissociates. However, a noticeable increase in bond length and bending of the CO_2 molecule after adsorption on the aforementioned sites of different surfaces shows that CO_2 might dissociate into CO at room temperature, which can subsequently be hydrogenated by the Ru-H surface species. Further, we investigated the adsorption of CO_2 on the surfaces that have already interacted with H_2 as shown in **Figure 6**. Since H_2 interaction with all the positive, negative, and neutral surfaces is more-or-less the same we considered only the negatively charged surfaces for this calculation. Multiple simulations were conducted whereby CO_2 was adsorbed (a) on physisorbed H_2 site A, (b) on surface OH formed from the splitting of H_2 on site B, and (c) on bare Ru formed by desorption of H_2O that resulted from the reaction of H_2 with surface O at Site C (Figure 5). The most interesting case is the one where CO_2 interacts with the surface OH groups and forms OCOH, a possible intermediate that may lead to formation of surface CO or C that can be further hydrogenated to form the main product CH_4 as observed in our experiments. A similar reaction mechanism was recently proposed by Sharma et al. who investigated the CO_2 methanation over ruthenium substituted CeO_2.[80] They also found that the substituted Ru was in the +4 oxidation state and the surface of the active catalyst consists of Ru and O, which is consistent with our observations. Overall, from the DFT studies, we conclude that H_2 splits on the surface of the RuO_2 to form hydroxyl groups, which then interact with the CO_2 to form intermediates, which ultimately lead to the formation of CH_4 as observed in our experiments.

3. Conclusion

We have developed a solution-phase technique to deposit nanostructured RuO_2 nanocrystals on 3D silicon photonic crystals, $ncRuO_2$/i-Si-o and investigated its activity toward gas-phase photomethanation of CO_2 with H_2 at ambient temperatures under high-intensity solar simulated light. The rate of CO_2 hydrogenation was an order of magnitude higher compared to when the RuO_2 was supported on a silicon wafer, $ncRuO_2$/SiW. DFT calculations were performed in order to understand the interaction of the reactants, CO_2 and H_2 with the photocatalyst and gain a deeper insight in the overall mechanistic details of the photomethanation process. The methanation process was activated via the interaction of H_2 with the oxygen of RuO_2 to form hydroxyl groups, which interacted with CO_2 to ultimately produce CH_4. The large surface area coupled with the unique light absorption properties of the photonic crystal was found to be responsible for the enhanced photomethanation rate. The ability of these highly absorbing nanostructured catalysts to utilize light and heat energy provided by the broadband solar irradiance to drive CO_2 reduction reactions represents an

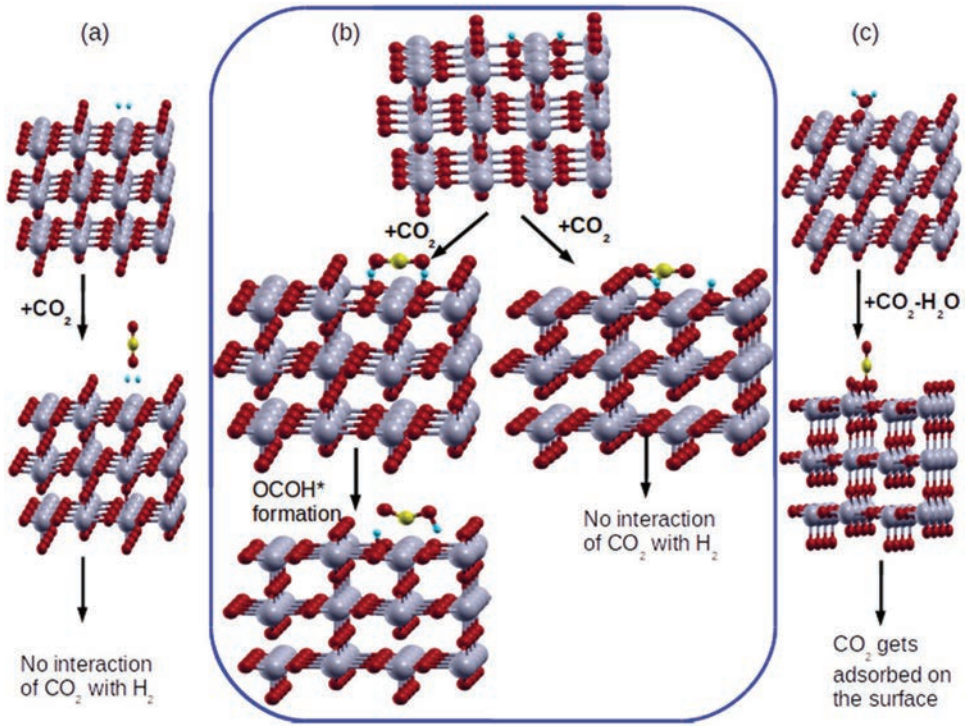

Figure 6. CO_2 adsorption on a) site A, b) site B, and c) site C of H_2 adsorbed $[Ru(110)]^{-1}$ surface. H, blue; C, yellow; Ru, gray and O, red.

important advancement that is applicable to a wide range of catalysts in the field of solar fuels.

4. Experimental Section

Fabrication of Inverse Silicon Opal Photonic Crystal Support: SiO_2 spheres with a diameter of ≈460 nm were first synthesized using a modified Stöber process and subsequently crystallized as SiO_2 opaline films using the evaporation-induced self-assembly (EISA) method on a polished silicon wafer with a surface area of ≈1 cm × 1 cm. The i-Si-o film was fabricated by infiltrating the interstitial voids in these SiO_2 films with amorphous silicon using a home-built dynamic chemical vapor deposition (CVD) apparatus and subsequently removing the SiO_2 template by etching in a solution containing HF. The attained i-Si-o films were then crystallized by subjecting them to an annealing treatment at a temperature of 630 °C for 5 h.

Deposition of Nanocrystalline RuO_2 on Inverse Silicon Opal Photonic Crystal Support: The deposition of $ncRuO_2$ onto the silicon inverse opal and the silicon wafer was done by wet chemical deposition. Each of these samples were first placed in 48% hydrogen fluoride solution for 1–2 min in order to remove any SiO_2 on the surface and to terminate the surface of these supports with hydrogen. The hydrogen-terminated silicon samples were placed in a solution containing 30 mg of $RuCl_2NO{\cdot}H_2O$ dissolved in 40 mL of water. This solution was then placed in a water bath heated to 40–45 °C and 3–5 drops of hydrazine was added to the solution to facilitate the reduction of ruthenium and formation of Ru NPs, which was later oxidized to RuO_2 NPs by heating it in an oven heated to 400 °C for 2 h. The concentration of the $RuCl_2NO{\cdot}H_2O$ solution was varied to achieve different RuO_2 sizes and loadings.

Gas-Phase Sabatier Reaction Rate Measurements: Gas-phase photocatalytic rate measurements were conducted in a custom-built 12 mL stainless steel batch reactor with a fused silica view port sealed with Viton O-rings (see Figure S10, Supporting Information). The sample dimensions used for the photocatalytic rate measurements were 1 cm × 1 cm. The pressure inside the reactor was monitored using an Omega PX309 pressure transducer. The duration of all runs was 2 h. Product gases were analyzed with a flame ionization detector (FID) and thermal conductivity detector (TCD) installed in a SRI-8610 Gas Chromatograph (GC) with a 3 in. Mole Sieve 13a and 6 in. Haysep D column. For heated tests, the reactor temperature was controlled by an OMEGA temperature controller combined with a thermocouple placed in contact with the rear side of the sample. The reactor was heated to 150 °C and purged with H_2 for 20 min prior to being infiltrated with CO_2 and H_2 at a H_2:CO_2 ratio of 4:1. For tests wherein the sample was irradiated with light, the lamp was turned on once the reactor valves were closed. The spectral output was measured using a StellarNet Inc. spectrophotometer and the power of the incident irradiation was measured using a Spectra-Physics power meter (model 407A).

Characterization of the Photocatalysts: SEM was used to study the morphology and structure of the samples. A Hitachi S-5200 SEM was used to study the surface topography of the samples. XPS measurements were carried out to study the surface and the electronic properties of the RuO_2 nanocrystals. XPS was performed in an ultrahigh vacuum chamber with base pressure of 10^{-9} mTorr. The system used a Thermo Scientific K-Alpha XPS spectrometer, with an Al Kα X-ray source operating at 12 kV, 6 A, and X-ray energy of 1486.7 eV. The spectra were obtained with analyzer pass energy of 50 eV with energy spacing of 0.1 eV. All data analysis was carried out using Thermo Scientific Avantage software.

Computational Details: The plane wave DFT implemented in Quantum ESPRESSO code[81] was used. The plane-wave pseudopotential approach, together with the Perdew–Burke–Ernzerhof (PBE)[82,83] exchange-correlation functional and Vanderbilt ultrasoft pseudopotentials,[84] was utilized throughout. All calculations are non-spin polarized. The kinetic energy cutoffs of 40 and 160 Ry were used for the smooth part of the electronic wave functions and augmented electron density, respectively. The self-consistent field convergence criterion was set to 1×10^{-6} Ry $Bohr^{-1}$ and the structures were relaxed using a conjugate gradient minimization algorithm until the magnitude

of residual Hellman–Feynman force on each atom was less than 10^{-3} Ry Bohr^{-1} for surfaces. Brillouin zone integrations were performed using a Monkhorst–Pack[85] grid of $4 \times 4 \times 1$ k points.

Supporting Information

Supporting Information is available from the Wiley Online Library or from the author.

Acknowledgements

G.A.O. is a Government of Canada Research Chair in Materials Chemistry and Nanochemistry. D.D.P. is the Celestica Chair in Materials for Microelectronics and co-director of the Ontario Centre for the Characterization of Advanced Materials (OCCAM). C.V.S. is the Erwin Edward Hart Endowed Professor of Materials Science and Engineering. Strong and sustained financial support for this work was provided by the Department of Materials Science and Engineering (MSE) at the University of Toronto, Ministry of Research Innovation (MRI), Ministry of Economic Development, Employment and Infrastructure (MEDI), Ministry of the Environment and Climate Change (MOECC), the Connaught Innovation Fund, the Connaught Global Challenge Fund, and Natural Sciences and Engineering Research Council of Canada (NSERC). The DFT simulations were conducted on the SciNet and Calcul-Quebec consortia through the Compute Canada. A.J. thanks Dr. Peter Brodersen and the Ontario Centre for the Characterization of Advanced Materials (OCCAM) for access to state-of-the-art surface analytical equipment and electron microscopic techniques. M.H. thanks K. A. Shair CRSL and the Masri Institute for Funding.

Conflict of Interest

The authors declare no conflict of interest.

Keywords

photochemical, photomethanation, photonic crystals, photothermal, solar fuels

Received: August 18, 2017
Revised: November 2, 2017
Published online: January 11, 2018

[1] M. A. A. Aziz, A. A. Jalil, S. Triwahyono, A. Ahmad, *Green Chem.* **2015**, *17*, 2647.
[2] J. L. White, M. F. Baruch, J. E. Pander, Y. Hu, I. C. Fortmeyer, J. E. Park, T. Zhang, K. Liao, J. Gu, Y. Yan, T. W. Shaw, E. Abelev, A. B. Bocarsly, *Chem. Rev.* **2015**, *115*, 12888.
[3] C. D. Windle, R. N. Perutz, *Coord. Chem. Rev.* **2012**, *256*, 2562.
[4] S. N. Habisreutinger, L. Schmidt-Mende, J. K. Stolarczyk, *Angew. Chem., Int. Ed.* **2013**, *52*, 7372.
[5] L. Yuan, Y.-J. Xu, *Appl. Surf. Sci.* **2015**, *342*, 154.
[6] W. Tu, Y. Zhou, Z. Zou, *Adv. Mater.* **2014**, *26*, 4607.
[7] W. Hou, W. H. Hung, P. Pavaskar, A. Goeppert, M. Aykol, S. B. Cronin, *ACS Catal.* **2011**, *1*, 929.
[8] M.-Q. Yang, Y.-J. Xu, *Nanoscale Horiz.* **2016**, *1*, 185.
[9] S. C. Roy, O. K. Varghese, M. Paulose, C. A. Grimes, *ACS Nano* **2010**, *4*, 1259.
[10] S. Neaţu, J. A. Maciá-Agulló, H. Garcia, *Int. J. Mol. Sci.* **2014**, *15*, 5246.
[11] Y. Izumi, *Coord. Chem. Rev.* **2013**, *257*, 171.
[12] Y.-F. Xu, M.-Z. Yang, B.-X. Chen, X.-D. Wang, H.-Y. Chen, D.-B. Kuang, C.-Y. Su, *J. Am. Chem. Soc.* **2017**, *139*, 5660.
[13] Y.-X. Pan, Y. You, S. Xin, Y. Li, G. Fu, Z. Cui, Y.-L. Men, F.-F. Cao, S.-H. Yu, J. B. Goodenough, *J. Am. Chem. Soc.* **2017**, *139*, 4123.
[14] W. Wang, S. Wang, X. Ma, J. Gong, *Chem. Soc. Rev.* **2011**, *40*, 3703.
[15] G. A. Olah, G. K. S. Prakash, A. Goeppert, *J. Am. Chem. Soc.* **2011**, *133*, 12881.
[16] W. Sun, C. Qian, L. He, K. K. Ghuman, A. P. Y. Wong, J. Jia, A. A. Jelle, P. G. O'Brien, L. M. Reyes, T. E. Wood, A. S. Helmy, C. A. Mims, C. V. Singh, G. A. Ozin, *Nat. Commun.* **2016**, *7*, 12553.
[17] L. B. Hoch, T. E. Wood, P. G. O'Brien, K. Liao, L. M. Reyes, C. A. Mims, G. A. Ozin, *Adv. Sci.* **2014**, *1*, 1400013.
[18] P. S. S. Prasad, J. W. Bae, K.-W. Jun, K.-W. Lee, *Catal. Surv. Asia* **2008**, *12*, 170.
[19] C. Zhao, L. Liu, Q. Zhang, J. Wang, Y. Li, *Catal. Sci. Technol.* **2012**, *2*, 2558.
[20] C.-C. Yang, J. Vernimmen, V. Meynen, P. Cool, G. Mul, *J. Catal.* **2011**, *284*, 1.
[21] F. Sastre, A. Corma, H. García, *J. Am. Chem. Soc.* **2012**, *134*, 14137.
[22] P. J. Lunde, F. L. Kester, *J. Catal.* **1973**, *30*, 423.
[23] C. Revilliod, J. A. McEvoy, M. Grätzel, *Sol. Energy Mater.* **1991**, *24*, 522.
[24] N. M. Gupta, V. S. Kamble, R. M. Iyer, K. R. Thampi, M. Gratzel, *Catal. Lett.* **1993**, *21*, 245.
[25] S.-T. Zhang, H. Yan, M. Wei, D. G. Evans, X. Duan, *RSC Adv.* **2014**, *4*, 30241.
[26] E. Zagli, J. L. Falconer, *J. Catal.* **1981**, *69*, 1.
[27] K. Ogura, M. Kawano, D. Adachi, *J. Mol. Catal.* **1992**, *72*, 173.
[28] F. W. Chang, M. S. Kuo, M. T. Tsay, M. C. Hsieh, *Appl. Catal., A* **2003**, *247*, 309.
[29] Y. Li, Q. Zhang, R. Chai, G. Zhao, F. Cao, Y. Liu, Y. Lu, *Appl. Catal., A* **2016**, *510*, 216.
[30] Y. Zhao, B. Zhao, J. Liu, G. Chen, R. Gao, S. Yao, M. Li, Q. Zhang, L. Gu, J. Xie, X. Wen, L.-Z. Wu, C.-H. Tung, D. Ma, T. Zhang, *Angew. Chem., Int. Ed.* **2016**, *55*, 4215.
[31] J.-N. Park, E. W. McFarland, *J. Catal.* **2009**, *266*, 92.
[32] M. Tahir, N. S. Amin, *Appl. Catal., A* **2015**, *493*, 90.
[33] C. Dai, A. Zhang, M. Liu, J. Li, F. Song, C. Song, X. Guo, *RSC Adv.* **2016**, *6*, 10831.
[34] C.-C. Lo, C.-H. Hung, C.-S. Yuan, J.-F. Wu, *Sol. Energy Mater. Sol. Cells* **2007**, *91*, 1765.
[35] K. R. Thampi, H. Kiwi, M. Grätzel, *Nature* **1987**, *327*, 506.
[36] J. Melsheimer, W. Guo, D. Ziegler, M. Wesemann, R. Schlögl, *Catal. Lett.* **1991**, *11*, 157.
[37] F. Sastre, A. V. Puga, L. Liu, A. Corma, H. García, *J. Am. Chem. Soc.* **2014**, *136*, 6798.
[38] P. G. O'Brien, A. Sandhel, T. E. Wood, A. A. Jelle, L. B. Hoch, D. D. Perovic, C. A. Mims, G. A. Ozin, *Adv. Sci.* **2014**, *1*, 1400001.
[39] L. B. Hoch, P. G. O'Brien, A. A. Jelle, A. Sandhel, D. D. Perovic, C. A. Mims, G. A. Ozin, *ACS Nano* **2016**, *10*, 9017.
[40] J. I. L. Chen, G. V. Freymann, S. Y. Choi, V. Kitaev, G. A. Ozin, *Adv. Mater.* **2006**, *18*, 1915.
[41] F. Ramiro-Manzano, P. Atienzar, I. Rodriguez, F. Meseguer, H. Garcia, A. Corma, *Chem. Commun.* **2007**, *3*, 242.
[42] Y. Li, T. Kunitake, S. Fujikawa, *J. Phys. Chem. B* **2006**, *110*, 13000.
[43] M. Ren, R. Ravikrishna, K. T. Valsaraj, *Environ. Sci. Technol.* **2006**, *40*, 7029.
[44] M. Srinivasan, T. White, *Environ. Sci. Technol.* **2007**, *41*, 4405.

[45] F. Sordello, C. Duca, V. Maurino, C. Minero, *Chem. Commun.* **2011**, *47*, 6147.
[46] F. Sordello, V. Maurino, C. Minero, *J. Mater. Chem.* **2011**, *21*, 19144.
[47] J. I. L. Chen, E. Loso, N. Ebrahim, G. A. Ozin, *J. Am. Chem. Soc.* **2008**, *130*, 5420.
[48] M. Curti, J. Schneider, D. W. Bahnemann, C. B. Mendive, *J. Phys. Chem. Lett.* **2015**, *6*, 3903.
[49] T. Suezaki, P. G. O'Brien, J. I. L. Chen, E. Loso, N. P. Kherani, G. A. Ozin, *Adv. Mater.* **2009**, *21*, 559.
[50] H. Y. H. Chan, C. G. Takoudis, M. J. Weaver, *J. Catal.* **1997**, *172*, 336.
[51] K. C. Park, I. Y. Jang, W. Wongwiriyapan, S. Morimoto, Y. J. Kim, Y. C. Jung, T. Toya, M. Endo, *J. Mater. Chem.* **2010**, *20*, 5345.
[52] L. T. Varghese, Y. Xuan, B. Niu, L. Fan, P. Bermel, M. Qi, *Adv. Opt. Mater.* **2013**, *1*, 692.
[53] H. Tan, E. Ye, W. Y. Fan, *Adv. Mater.* **2006**, *18*, 619.
[54] S. Bang, S. Lee, T. Park, Y. Ko, S. Shin, S.-Y. Yim, H. Seo, H. Jeon, *J. Mater. Chem.* **2012**, *22*, 14141.
[55] A. Belkind, Z. Orban, J. L. Vossen, *Thin Solid Films* **1992**, *207*, 242.
[56] D. Ugur, A. J. Storm, R. Verberk, J. C. Brouwer, W. G. Sloof, *J. Phys. Chem. C* **2012**, *116*, 26822.
[57] G. A. White, T. R. Roszkowski, D. W. Stanbridge, *Adv. Chem. Ser.* **1975**, *146*, 138.
[58] R. L. Ensell, H. J. F. Stroud, presented at *Proc. 1983 Int. Gas Res. Conf.* London, June **1983**.
[59] J. Gao, Y. Wang, Y. Ping, D. Hu, G. Xu, F. Gu, F. Su, *RSC Adv.* **2012**, *2*, 2358.
[60] D. C. Upham, A. R. Derk, S. Sharma, H. Metiu, E. W. McFarland, *Catal. Sci. Technol.* **2015**, *5*, 1783.
[61] M. R. Prairie, A. Renken, J. G. Highfield, K. R. Thampi, M. Grätzel, *J. Catal.* **1991**, *129*, 130.
[62] S. Eckle, H.-G. Anfang, R. J. Behm, *J. Phys. Chem. C* **2011**, *115*, 1361.
[63] S. Akamaru, T. Shimazaki, M. Kubo, T. Abe, *Appl. Catal., A* **2014**, *470*, 405.
[64] B. Miao, S. S. K. Ma, X. Wang, H. Su, *Catal. Sci. Technol.* **2016**, *6*, 4048.
[65] J. Gao, Q. Liu, F. Gu, B. Liu, Z. Zhong, F. Su, *RSC Adv.* **2015**, *5*, 22759.
[66] T. Abe, M. Tanizawa, K. Watanabe, A. Taguchi, *Energy Environ. Sci.* **2009**, *2*, 315.
[67] D. Li, N. Ichikuni, S. Shimazu, T. Uematsu, *Appl. Catal., A* **1999**, *180*, 227.
[68] A. Kim, C. Sanchez, G. Patriarche, O. Ersen, S. Moldovan, A. Wisnet, C. Sassoye, D. P. Debecker, *Catal. Sci. Technol.* **2016**, *6*, 8117.
[69] S. Carenco, C. Sassoye, M. Faustini, P. Eloy, D. P. Debecker, H. Bluhm, M. Salmeron, *J. Phys. Chem. C* **2016**, *120*, 15354.
[70] F. Hai-Bo, Y. Shao-Yan, Z. Pan-Feng, W. Hong-Yuan, L. Xiang-Lin, J. Chun-Mei, Z. Qin-Sheng, C. Yong-Hai, W. Zhan-Guo, *Chin. Phys. Lett.* **2007**, *24*, 2108.
[71] X. Zhang, J. Qin, Y. Xue, P. Yu, B. Zhang, L. Wang, R. Liu, *Sci. Rep.* **2014**, *4*, 4596.
[72] A. Ganguly, S. Sharma, P. Papakonstantinou, J. Hamilton, *J. Phys. Chem. C* **2011**, *115*, 17009.
[73] A. Jelle, M. Hmadeh, P. G. O'Brien, D. D. Perovic, G. A. Ozin, *ChemNanoMat* **2016**, *2*, 1047.
[74] D. Rochefort, P. Dabo, D. Guay, P. M. A. Sherwood, *Electrochim. Acta* **2003**, *48*, 4245.
[75] C. Xu, Y. Jiang, D. Yi, H. Zhang, S. Peng, J. Liang, *J. Am. Ceram. Soc.* **2014**, *97*, 3702.
[76] K. Reuter, M. Scheffler, *Phys. Rev. B* **2001**, *65*, 035406.
[77] H.-S. D. Kim, J. Yang, Y. Qi, A. M. Rappe, *J. Phys. Chem. C* **2017**, *121*, 1585.
[78] K. Reuter, M. Scheffler, *Phys. Rev. B* **2003**, *68*, 045407.
[79] R. F. W. Bader, P. J. MacDougall, *J. Am. Chem. Soc.* **1985**, *107*, 6788.
[80] S. Sharma, K. B. S. Kumar, Y. M. Chandnani, V. S. P. Kumar, B. P. Gangwar, A. Singhal, P. A. Deshpande, *J. Phys. Chem. C* **2016**, *120*, 14101.
[81] P. Giannozzi, S. Baroni, N. Bonini, M. Calandra, R. Car, C. Cavazzoni, D. Ceresoli, G. L. Chiarotti, M. Cococcioni, I. Dabo, A. D. Corso, S. D. Gironcoli, S. Fabris, G. Fratesi, R. Gebauer, U. Gerstmann, C. Gougoussis, A. Kokalj, M. Lazzeri, L. Martin-Samos, N. Marzari, F. Mauri, R. Mazzarello, S. Paolini, A. Pasquarello, L. Paulatto, C. Sbraccia, S. Scandolo, G. Sclauzero, A. P. Seitsonen, A. Smogunov, P. Umari, R. M. Wentzcovitch, *J. Phys.: Condens. Matter* **2009**, *21*, 395502.
[82] J. P. Perdew, K. Burke, M. Ernzerhof, *Phys. Rev. Lett.* **1996**, *77*, 3865.
[83] J. Muscat, A. Wander, N. M. Harrison, *Chem. Phys. Lett.* **2001**, *342*, 397.
[84] D. Vanderbilt, *Phys. Rev. B* **1990**, *41*, 7892.
[85] H. J. Monkhorst, J. D. Pack, *Phys. Rev. B* **1976**, *13*, 5188.

